Aflatoxins detection in almonds via fluorescence imaging and deep neural network approach

Francesca Romana Bertani [a],[1], Arianna Mencattini [b],[2], Lucia Gambacorta [c],[3], Adele De Ninno [a],[4], Luca Businaro [a],[5], Michele Solfrizzo [c],[6], Annamaria Gerardino [a],[*],[7], Eugenio Martinelli [b],[8]

[a] CNR Institute for Photonics and Nanotechnologies, via del Fosso del Cavaliere 100, 00133 Rome, Italy
[b] Department of Electronic Engineering, University of Rome Tor Vergata, via del Politecnico 1, 00133 Rome, Italy
[c] CNR Institute of Sciences of Food Production, via Amendola, 122/O, 70126 Bari, Italy

ARTICLE INFO

ABSTRACT

The detection of aflatoxin B in raw food materials represents a topic of great interest worldwide because of the huge health and economic impact of aflatoxin contamination. In this paper, we present an original approach to aflatoxin detection, using a portable instrument to acquire fluorescence images, among other spectral responses. The acquired images are processed by combining a color space conversion from the RGB scale to Y′CbCr, and a neural network approach to encode a vector of features. After a feature reduction using a Receiving Operating Curve method, two-class and three-class classification tasks of contaminated vs non-contaminated samples are accomplished. This procedure has been applied to artificially contaminated grained almond samples in the range of 0–320.2 ng/g, achieving an overall classification accuracy between 84.7% and 93.0%, depending on the number of classes. Thus, in this setting, we show that good classification performance can be achieved using only an image acquisition and analysis approach. The proposed procedure can represent a cheap, rapid, non-destructive yet sensitive method for the assessment of aflatoxin B contamination in food matrices, and its monitoring and tracing throughout the food chain.

1. Introduction

Aflatoxins (AFs) are toxic secondary metabolites mostly produced by the fungi *Aspergillus flavus, Aspergillus parasiticus* and *Aspergillus nomius* (Fernández-Ibañez et al., 2009), that have a strong negative impact on crops and food. There are four major types of aflatoxins, AFB_1 ($C_{17}H_{12}O_6$), AFB_2 ($C_{17}H_{14}O_6$), AFG_1 ($C_{17}H_{12}O_7$) and AFG_2 ($C_{17}H_{14}O_7$), highly toxic due to their deleterious effects on humans and animals, and AFB_1 is the most common and dangerous one. The classification in 'B′' and 'G′' types, refers to the blue and green fluorescence emission produced by these compounds under UV light illumination. Numbers 1 and 2 indicate major and minor compounds, respectively (Hussein and Brasel, 2001; Weidenbörner, 2001). The interest in methods for detecting AFs contaminations in a rapid, very sensitive, and non-destructive way is currently increasing as it is important to control food safety along the entire food production chain, and ensure health and economic benefits. In fact, AFs are known carcinogens, associated with liver and lung cancer in humans, and immunosuppressive agents (Benkerroum, 2020; IARC, 1993). AFs are also found in several kinds of food commodities, like cereals (i.e. corn, soybean, wheat, maize, and rice), nuts, and dried fruits. AFs may be produced at various stages of the food chain: before harvest in fields, during the harvest process, and

* Correspondence to: CNR-IFN, via del Fosso del Cavaliere 100, 00133 Roma, Italy.
  E-mail address: annamaria.gerardino@cnr.it (A. Gerardino).
[1] ORCID 0000-0001-6529-8993
[2] ORCID 0000-0002-3753-0457
[3] ORCID 0000-0002-8870-8198
[4] ORCID 0000-0003-3139-2820
[5] ORCID 0000-0002-5251-093X
[6] ORCID 0000-0002-5698-4921
[7] ORCID 0000-0003-1869-1092
[8] ORCID 0000-0002-6673-2066

during storage or transportation. Therefore, the availability of portable sensors capable of detecting the presence of AFs along the entire food chain is of great importance. In addition to cereal contamination, the presence of AFB_1 can be detected in oilseeds such as peanuts, almonds, walnuts, and sesame seeds (Bhat and Reddy, 2017), and also in products such as chili peppers. Due to the above, about 120 countries worldwide regulate AFs levels in food and feed (Jallow et al., 2021). In the USA, AFs levels in food and feed products are regulated by the Food and Drug Administration (FDA, 2000) which sets the limits of contamination levels at 20 ng/g or more, depending on the food commodity, while the European legislation has set limits as low as 8 ng/g for AFB_1 in almonds, and 10 ng/g for total AFs (Commission Regulation (EC), 2006). In the European Union there are several actions and projects focused on the detection and management of mycotoxins (and aflatoxins in particular), such as the Mycokey (www.mycokey.eu), MycoTwin (www.mycotwin. eu), and MyToolBox (www.mytoolbox.eu) projects.

Furthermore, climate change has been reported to be a driver of emerging food and feed safety issues worldwide, and its expected impact on the presence of mycotoxins, and AFs in particular, in food and feed is of great concern (Battilani et al., 2016). Currently, AFs detection and quantification methods are based on analytical tests, including mass spectrometry, gas chromatography, thin-layer chromatography, high-performance liquid chromatography, and enzyme-linked immunosorbent assays (Köppen et al., 2010; Singh and Mehta, 2020). These methods are characterized by high detection accuracy and specificity, but require the destruction of samples, and are not suitable for field detection. Moreover, such procedures are costly, time consuming, and require specialized personnel to perform the analysis. Thus, the ability to detect AFs in a rapid, specific, non-destructive, and easy way represents a challenge for several food industries and control bodies. Several methods have been proposed in this perspective, mainly based on optical methods like spectroscopy and imaging (Tao et al., 2018).

Spectral approaches have shown very good results, the most promising being fluorescence spectroscopy, near infrared spectroscopy, and hyperspectral imaging. These approaches require optimization of the acquisition conditions, and appropriate chemometric models to analyze the results. Recent progress in machine learning-based data analysis greatly improved the classification ability of models based on acquired data and allows for trustable detection systems (Bartolić et al., 2022; Chakraborty et al., 2021; Han and Gao, 2019; Zhou et al., 2021). Imaging approaches are of utmost importance to inspect many different food commodities as accurately and rapidly as possible, and in a non-invasive way: several imaging approaches have been explored over the last few years, mostly involving hyperspectral imaging in different spectral ranges. Since AFs usually have a superficial or surface distribution, these approaches have been widely applied recently (Kimuli et al.,2018; Zhongzhi, 2019; Zhongzhi and Limiao, 2020; Zhu et al., 2016), again in combination with machine learning analysis methods. It must be underlined that very powerful, hyperspectral imaging is expensive from a point of view of data acquisition and processing power. Moreover, data extraction is not always straightforward, especially in the context of food analysis and processing (Ravikanth et al., 2017). Therefore, the possibility of using alternative imaging techniques, that are cheaper and faster, can be of great interest for the on-field and on-line detection of AFs contamination (Wu et al., 2018; Wu and Xu, 2020).

The possibility of using fluorescence imaging can represent a valid alternative to hyperspectral approaches, but proper image pre-processing is needed to select the most significant features. As an example, the autofluorescence of the food matrices may produce contributions that are possibly misleading, and this event must be taken into account. In this paper, we present a portable optical system based on an RGB CMOS camera, with UV LED illumination, and a novel processing strategy to analyze fluorescence images. By exploiting a change of color scale and then applying a deep neural network approach, we can highlight better the information needed to discriminate even small AFs

concentration levels. Almond samples artificially contaminated with AFs can be classified with an accuracy of up to 90%. Notably, all that is needed to acquire the fluorescence images is a CMOS camera and a UV LED illumination at 375 nm, so that a sensor fully dedicated to fluorescence imaging can be achieved in a portable, very simple, and non-expensive manner.

2. Materials and methods

2.1. Production of AF-contaminated almonds

To establish a calibration curve, we prepared a series of contaminated almond substrates using a procedure that mimics natural contamination. The shelled almonds (cultivar Genco, farm Marilù Perrone, Conversano, BA, Italy) were inoculated with a strain of Aspergillus flavus (ITEM 7828, available in the fungal collection of the Institute for Science of Food Production - Italian National Research Council, ISPA-CNR) that produces only Aflatoxin B_1 and B_2, according to the experimental conditions reported elsewhere (Bertani et al., 2020; Zivoli et al., 2014). Different aliquots of this contaminated sample were mixed with blank ground almonds to prepare 9×80 g of ground almonds containing different levels of AFB_1 and AFB_2. All almond samples were slurred for 5-min with 160 ml of water, freeze-dried, ground, and analyzed by HPLC-FLD (high-performance liquid chromatography with fluorescence detector) to measure accurately the levels of AFB_1 and AFB_2 (limit of detection 0.2 ng/g). The HPLC-FLD analyses were performed with an Agilent 1100 series (Agilent Technologies, Inc., Wilmington, DE, USA), consisting of a binary pump (G1312A), an autosampler (G1313A) with a 100 μL loop, a fluorescence detector (G1321A) fixed at 365 nm λ_{ex} and 435 nm λ_{em}, a thermostatic column oven set at 30 °C, and software for Microsoft Windows 2000 (HP ChemStation). The column used was a 150 mm × 4.6 mm i.d., 3 μm, Luna PFP (2) (pentafluorophenyl-propyl) (Phenomenex, Torrance, CA, USA) with a 3 mm i.d., 0.45 μm pore size guard filter (Rheodyne, Cotati, CA, USA). The results of AFB_1 and AFB_2 levels measured in the 9 samples of ground almonds and in the control samples are reported in Table 1. We underline that 5 out of the 9 samples have a contamination level ≤ 10 ng/g, which is the EU limit for total AFs in almonds, pistachios, and apricot kernels intended for direct human consumption or use as an ingredient in foodstuffs.

2.2. Image acquisition

The image data set was acquired in a measurement campaign performed in spring 2021 at the premises of the Institute for Photonics and Nanotechnologies - Italian National Research Council, IFN-CNR. Images were acquired on ground samples using a custom-built portable sensor prototype (Georgoulas et al., 2019; Groß et al., 2019) developed within the framework of the EU H2020 PhasmaFOOD project (www.phasmafood.eu). During a single measurement run, several spectroscopic signals and images were acquired from the same spot: UV excited

Table 1
Levels of AFB_1 and AFB_2 in samples of ground almonds used in this study. ND: not detected (LOD: 0.2 ng/g).

Sample	AFB_1 (ng/g)	AFB_2 (ng/g)	$AFB_1 + AFB_2$ (ng/g)
Almond 1 (Control, uncontaminated)	ND	ND	
Almond 2	291 ± 8.7	29.2 ± 1.5	320.2 ± 8.9
Almond 3	39.3 ± 1.2	5.9 ± 0.2	45.2 ± 1.2
Almond 4	16.4 ± 0.5	1.9 ± 0.1	18.3 ± 0.5
Almond 5	12.5 ± 0.4	1.2 ± 0.06	13.7 ± 0.4
Almond 6	9.9 ± 0.3	0.8 ± 0.04	10.7 ± 0.3
Almond 7	8.3 ± 0.2	0.6 ± 0.03	8.9 ± 0.3
Almond 8	6.0 ± 0.2	0.4 ± 0.02	6.4 ± 0.2
Almond 9	4.2 ± 0.1	0.2 ± 0.01	4.4 ± 0.1
Almond 10	2.6 ± 0.1	0.1 ± 0.01	2.7 ± 0.1

fluorescence spectra, diffuse reflectance spectra in the visible (VIS) and near-infrared (NIR) range, together with fluorescence, VIS and NIR images. The prototype integrates a UV–VIS mini-spectrometer (C12880MA, HAMAMATSU PHOTONICS K.K., Hamamatsu City, Japan), an NIR mini-spectrometer, prototype from IPMS Fraunhofer Institute (Pügner et al., 2016), and a miniaturized RGB CMOS camera (MU9PC-MH, XIMEA GmbH, Münster, Germany). The illumination sources consist of white-light LEDs (Mini Toppled LCW MVSG.EC, Osram GmbH, Munich, Germany), Xenon-based micro-lamps (MGG 8321–700-B2), and two UV LEDs emitting at 375 nm (NSSU100DT, Nichia Corporation, Tokushima, Japan). Optical filters to select excitation spectral bands were included as well, namely a band pass filter in front of the UV LEDs (360/23 BrightLine HC, Semrock Inc, Rochester, NY, USA), with a wide pass band centered at 360 nm, and a specified blocking optical density (OD) of 6. The prototype measurement geometry ensured a fixed distance between the surface of the sample, and the CMOS camera and the other sensors. For the acquisition of fluorescence images, the integration time for the camera was set at 3 s, after fixing at 15 mA the current supply to the UV LED to obtain a stable emission. Images were acquired in a single shot, in a jpg image file format with a resolution of 2592 × 1944 Pixels (5.04 MPixels).

For each level of contamination, two duplicates of the sample were prepared, splitting the grained almonds into separate Petri dishes, and identified as 'A' and 'B' samples. At least 30 images for each contamination level were acquired (different spots on the same sample to take into consideration the food matrix inhomogeneity), and after a preselection step, a total of 300 images (157 'A' sample set and 143 'B' sample set) were included in the dataset. Proper shielding from environmental light was ensured throughout all acquisitions.

2.3. Image analysis

The analysis of the acquired images is structured into four main steps: image preprocessing (Fig. 1), image encoding by transfer learning (Fig. 2), two-class pattern recognition by optimized Linear Discriminant Analysis (LDA) (Fig. 3), and three-class recognition by optimized LDA (Fig. 4).

2.4. Image preprocessing

The original images present a large area, and only a limited part of it is illuminated by LED sources. Moreover, during acquisition, in some cases the edges of the Petri dishes containing the sample were illuminated partially and their reflection appears in the resulting image in the form of greenish components (Fig. 1).

To standardize the images, an automatic crop of the image was performed around the center of the illumination spot by extracting a square region of 500 × 500 pixels. This step enabled also to reduce artifacts that may have occurred due to reflections of the excitation LEDs (bright spots in the top left and right corners on the left side of Fig. 1). Each squared image was then subjected to a color transformation
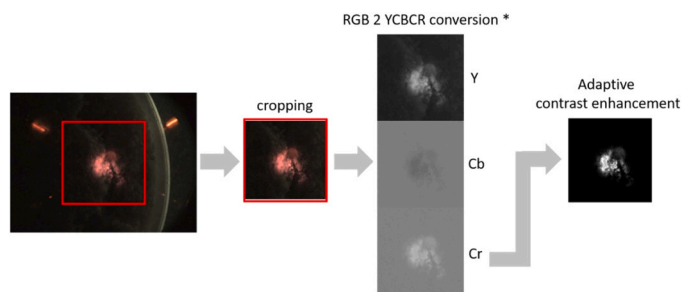
processing from RGB to Y′CbCr color space (Poynton, 1996). The Y′CbCr space is a family of color spaces used as a part of the color image pipeline in video and digital photography systems. Y ′ is the so-called luma component which is derived by the luminance (the greyscale conversion of the RGB image) by nonlinear gamma correction, while Cb and Cr are the blue-difference and red-difference chroma components. Being a relative color space, Y′CbCr is useful to ensure uniformity, and in our context, the Cr component is fundamental to eliminate the presence of the green shadow on the background. After preliminary simulations, the Y′CbCr color domain was preferred over others, such as the Hue Saturation Value (HSV). This approach determined an improvement of the statistical robustness of the results counteracting the possible fluctuation of the experimental set-up conditions. The contrast-enhanced version of the derived Cr image is shown on the right part of Fig. 1 (Gonzalez and Woods, 2007).

2.5. Image encoding by transfer learning

Each image, transformed as described above, is sent to a pre-trained Convolutional Neural Network (CNN) with the aim of extracting an automatic image encoding signature. To do this, we exploited the CNN ShuffleNet (Zhang et al., 2017), as shown in Fig. 2. The selected network demonstrated to be an extremely computation-efficient CNN architecture specifically designed for mobile devices with very limited computing power. The architecture utilizes two new operations, pointwise group convolution and channel shuffle, to greatly reduce computation costs while maintaining accuracy. During simulations, the performance of ShuffleNet has been compared with well-known Deep Learning architectures such as Alexnet (Russakovsky et al., 2015) and Resnet101 (He et al., 2016), demonstrating to be superior in the accuracy of classification. By using a pre-trained CNN, we avoided not only overlearning problems, and the consequent need to augment the training dataset, but also reinforced the robustness of the platform for the analysis of food quality by a network reuse paradigm. Each image is coded into a vector of numerical descriptors extracted at a specific network layer. More in detail, we used the layer node_161 of the ShuffleNet that returns a code vector of 13328 features. Among the pooling layers in the ShuffleNet architecture (node-4, node-15, node-64, node-161, and node-200) node-161 was an acceptable trade-off between the number of features extracted and the achieved performance.

2.6. Two-class classification problem

In order to recognize automatically the presence of AFs in the samples, we outlined a two-class problem in which we defined as class 0 all images with a concentration of AFs below the limit of detection of HPLC measurement (LOD: 0.2 ng/g), which we named conventionally as 0 ng/g, and as class 1 all remaining images ($\geq$2.7 ng/g). A cross-validation procedure based on a sample-out logic was implemented using in turn images from sample set'A' and from sample set 'B' from all concentrations, for the training and testing steps respectively.

The high number of features extracted made it necessary to implement an automatic feature selection procedure. In particular, we implemented a supervised AUC-based algorithm in which the Area
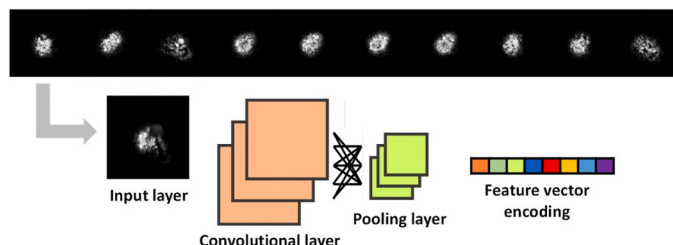

Fig. 1. Preprocessing steps followed for each image analyzed: Crop, Color Space Conversion, Contrast Enhancement.

Fig. 2. Image encoding procedure using CNN: ShuffleNet.

Under the roC (AUC) (Zweig and Campbell, 1993) value of each feature is calculated over the training dataset and used to select only the most significant features. Very high or very low AUC values are indicative of a high discrimination ability. The most significant features are used to construct a Linear Discriminant Analysis (LDA) model (McLachlan, 2004) to recognize class 0 samples from class 1 ones (Fig. 3).

2.7. Three-class classification problem

The wide range of contamination levels (0–320.2 ng/g) suggests the need to perform also a three-class recognition task in which we identified three distinct categories: class 0 (uncontaminated samples),; class 1 (moderately contaminated samples), concentration (2.7 – 18.3 ng/g); class 2 (relevantly contaminated samples), concentration > 18.3 ng/g. The AUC-based method is standardly thought for a two-class problem, because the AUC value is directly related to the capacity to discriminate samples in a given distribution by using a single threshold value. In this case, we adapted the approach to the three-class problem by the following two-step procedure: first, we calculated the AUC of features discriminating class 0 from the others, and we denoted this value as AUC_{low}. Then, we repeated the procedure by calculating the AUC values of features discriminating class 2 from the others, and we denoted this value as AUC_{high}. Finally, we collected the combination of the feature sets selected by using independently AUC_{low} and AUC_{high} criteria.

The selected features are used to construct a three-class LDA model using the cross-validation strategy already implemented in the two-class problem, as shown in Fig. 4.

2.8. Data analysis details

The data analysis has been performed using Matlab 2020b (Math-Works, Natick, MS, USA) using an Intel core i7, 9th generation, with the following characteristic processing times:

- Average time required to pre-process each image is 0.05 s,
- Average time to encode each image by transfer learning is 0.73 s
- Time needed for the AUC calculation is 13.70 s
- Time required to construct the model and classify the test partition is 0.37 s

3. Results and discussion

The results of the developed classification algorithms are visualized by confusion matrices. We recall that the total image data set consists of 300 images, 157 from the 'A' sample set and 143 from the 'B' sample set.

3.1. Two-class recognition

In the two-class classification problem, we considered two case studies. In Case study 1, the 143 images of the 'B' sample set were used to train the algorithm, and the 157 images of the 'A' sample set were used to test it. Of the test images, 15 have no detectable contamination, and the remaining 142 images have contamination levels ≥ 2.7 ng/g. As previously defined, class 0 identifies uncontaminated samples and class

1 contaminated samples (contamination ≥ 2.7 ng/g). The corresponding confusion matrix is shown in Fig. 5(a).

93.0% of the samples are correctly classified, and only 11 samples are misclassified (7.0%). In this last group, false negatives (contaminated samples classified as non-contaminated, i.e. the most alarming ones) correspond to contaminations that are mostly below the EU maximum permitted levels (2.7,4.4,4.4,4.4,8.9,13.7 ng/g).

Case study 2, instead, used images from the 'A' sample set as the training set, and images from the 'B' sample set as the testing set. In this case, the testing set is composed of 15 images of not contaminated samples (Class 0) and 128 images with contamination ≥ 2.7 ng/g (Class 1). The results are summarized in the confusion matrix shown in Fig. 5 (b). It is interesting to note that the overall classification rate is 91.6%, while 8.4% of the misclassified samples are assigned almost equally to the two classes.

3.2. Three-class recognition

Regarding the three-class recognition problem, again two case studies were analyzed considering alternatively the datasets from sample sets 'A' and 'B' as training and testing sets. In this case, we defined class 0 as uncontaminated samples, class 1 as samples with contamination 2.7 ng/g $\leq$ C $\leq$ 18.3 ng/, and class 2 as samples with contamination ≥ 40.0 ng/g.

In Case study 1, the sample set 'A' images used to test the classification algorithm consist of 15 images of uncontaminated samples, 110 images of samples with contamination levels ≥ 2.7 ng/g and ≤ 18.3 ng/g, and 32 images of samples with contamination level > 18.3 ng/g. Fig. 6 shows the confusion matrix of the three-class problem, Case study 1. 84.7% of the samples are correctly classified, and 15.3% are misclassified. However, considering the negative (uncontaminated) classified row, only 3.2% are false negative samples, with a contamination level < 18.3 ng/g. None of the highly contaminated samples were classified as negative.

Case study 2, represented by the confusion matrix shown in Fig. 7, presents 90.9% of correctly classified images and 9.1% of misclassified ones. In this case, the sample set 'A' images have been used to train the algorithm, and sample set 'B' images to test it. Among sample set 'B' images, 15 are of uncontaminated samples, 100 images are from contamination levels ≥ 2.7 ng/g and ≤ 18.3 ng/g, and 28 images are from samples with contamination > 18.3 ng/g. Also in this case, the first row of the confusion matrix, corresponding to the images classified as uncontaminated, shows that only four images are classified as false negative samples (2.8%), and no images of the highly contaminated (>18.3 ng/g) samples are classified as negative ones.

The overall performance of the analysis is very good: in the worst case, we have an 84.7% classification accuracy (three-class classification task, Case study 1), and in the best one, we have 93.0% of correctly classified images (two-class classification task, Case study 1). Notably, samples classified as false negatives in most cases have a contamination level lower than the EU limit for total AFs in almonds.

It is also worth highlighting that the applied transformation of images from RGB to Y'CbCr to improve reproducibility is original in this field of mycotoxin detection. To the best of our knowledge, the RGB to
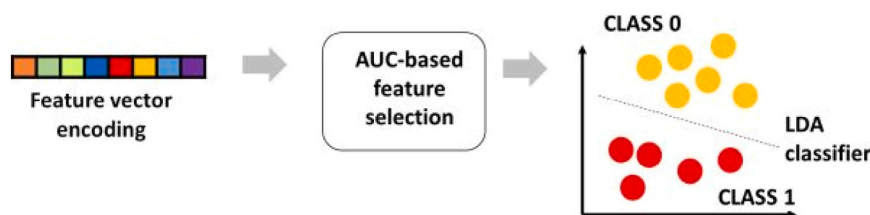

Fig. 3. Two-class classification task. Starting from the feature vector extracted from each image in the training set, an Area Under the roC (AUC)-based feature selection criterion was used, and a Linear Discriminant Analysis (LDA) architecture was trained and applied for automatic sample recognition.
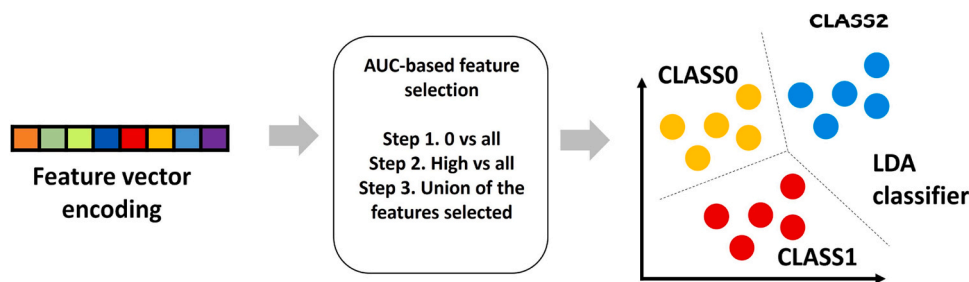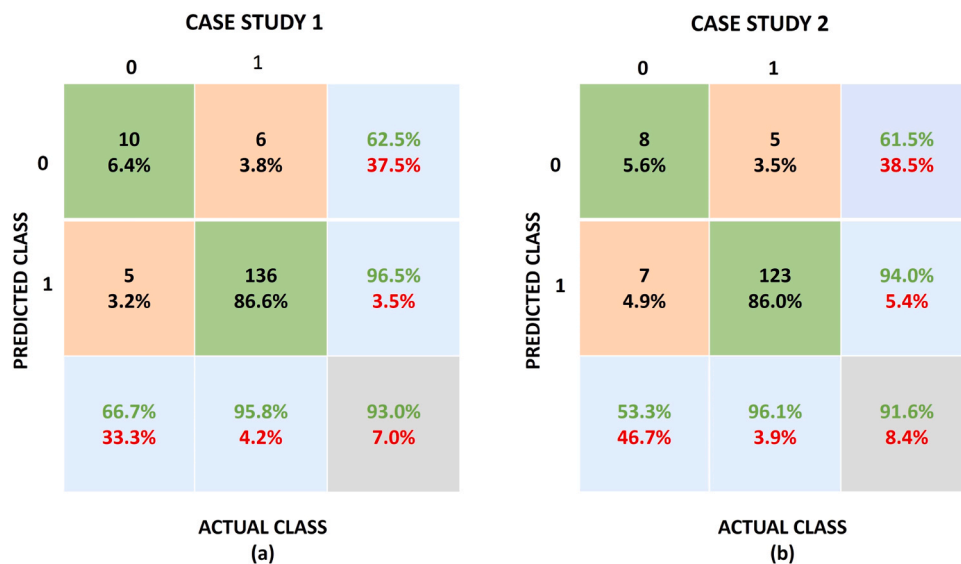
Fig. 4. Three-class classification task. Starting from the feature vector extracted from each image in the training set, a novel two-step Area Under the roC (AUC)-based feature selection criterion was used, and a Linear Discriminant Analysis (LDA) architecture was trained and applied for automatic sample recognition.

Fig. 5. Confusion matrices for two-class classification tasks. Class 0: uncontaminated; Class 1: contamination$\geq$ 2.7 ng/g. (a) Case study 1. Testing set: 157 Images from sample set 'A', Training set: 143 Images from sample set 'B'. (b) Case study 2. Testing set: 143 Images from sample set 'B ', Training set: 157 Images from sample set 'A'. The green boxes are the True Negative and True Positive outputs, i.e., the rightly classified samples. Orange ones are False Positives and False Negatives. The light-blue boxes report the percentages of rightly (in green) and wrongly (in red) classified samples for each column/row. The grey box reports the overall rightly (in green) and wrongly (in red) classified samples.
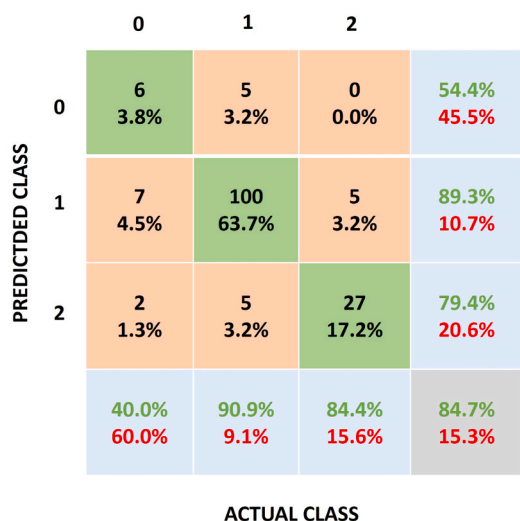

Fig. 6. Confusion matrix for three-class classification task, Case study 1. Class 0: uncontaminated samples; Class 1: contamination 2.7 ng/g $\leq$ C $\leq$ 18.3 ng/g; Class 2 contamination $\geq$ 40.0 ng/g. Testing set: 157 images from sample set 'A'. Training set: 143 images from sample set 'B'. For the confusion matrix legend, see Fig. 5.
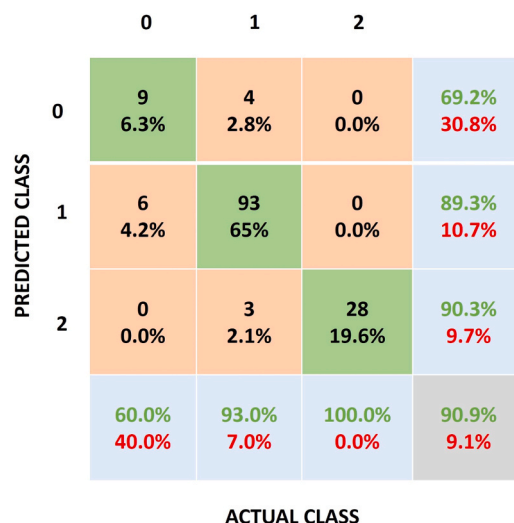
Fig. 7. Confusion matrix for three-class classification task, Case study 2. Class 0: uncontaminated samples; Class 1 contamination 2.7 ng/g $\leq$ C $\leq$ 18.3 ng/g; Class 2 Contamination $\geq$ 40.0 ng/g. Testing set: 143 Images from sample set 'B'. Training set: 157 Images from sample set 'A'. For the confusion matrix legend, see Fig. 5.

Y′CbCr color space conversion has been used in limited applications for food analysis (Liu et al., 2019).

The approach proposed in this work is clearly different from the literature. Although there are similar works for some aspects, with regard to the specific application and use of fluorescence (Lunadei et al., 2013) and the processing adopted (Pareek et al., 2023), the potential of deep learning and adequate processing to achieve high-performance with a low-cost measurement system, has not been exploited so-far.

When comparing with the approach proposed by Lunadei et al. (2013), also based on fluorescence imaging, where the light source was provided by six Wood lamps, which are much more expensive than the UV LEDs used in our approach, the image acquisition was performed in a multispectral imaging configuration that is more data and time-consuming. Finally, the analysis was performed on single seeds from highly contaminated batches (190 ng/g for pistachio nuts), while in our case, thanks to the use of processing based on deep neural networks, the system is able to classify contamination values of the grained almonds around the EU-allowed limits (10 ng/g).

Pareek et al., 2023, propose a similar approach for data processing, based on RGB image color conversion (in their case is RGB -> HSV), feature selection based on Ant Colony Optimization algorithm, and a multilayer perceptron neural network (MLPNN) for the classification task. In their work, the data analysis approach is applied to visible images of maize kernels with the aim of separating whole kernels from the broken ones, and the classification task is applied to morphological issues.

The novelty of our work rests in all those differences that, with a relatively low-cost system, enable to obtain performances comparable with much more expensive techniques that represent the current state-of-the-art for this kind of application.

Although the results obtained exploiting the new color space domain are very promising, more extensive experimental studies should be performed. Aspects such as new Neural Networks processing should be investigated, and new experiments should be planned where on-the-field naturally AFs-contaminated samples, and/or additional kinds of contaminations, will be considered.

4. Conclusions

The main objective of this paper is to demonstrate the possibility of detecting aflatoxin contamination in almond samples, even at very low levels, in a fast, cost-effective, and non-invasive way, simply by using fluorescence imaging combined with a deep neural network approach. To achieve this we considered a set of artificially aflatoxin B-contaminated almond samples: the acquired fluorescence images were processed by converting the color space from the RGB scale to Y′CbCr and then using a neural network approach to perform a two-class and a three-class classification problem. The best classification accuracy obtained in the two-class problem is 93.0% and in the three-class problem is 90.9%, suggesting that fluorescence imaging can be considered as a tool for the rapid screening of food matrices for the presence of AFs. The fluorescence images were acquired using only UV LEDs and an RGB CMOS camera in a suitable arrangement, providing a low-cost and sensitive sensor that can be employed in any applications where a rapid, on-field and non-destructive testing is required. Previously, we demonstrated the feasibility of fluorescence spectroscopy as a tool for the detection of AFs in almonds in a very simple and portable setup with classification accuracies up to 94.0%, and with a threshold set at 6.4 ng/g (Bertani et al., 2020). As a further development of our research on portable optical methods for the identification of AFs in food matrices, the fusion of data coming from spectroscopic and imaging techniques will be implemented to make the classification model more robust.

Funding

CRediT authorship contribution statement

Declaration of Competing Interest

None.

Data Availability

Data will be made available on request.

Acknowledgment

References

Bartolić, D., Mutavdžić, D., Carstensen, J.M., Stanković, S., Nikolić, M., Krstović, S., Radotić, K., 2022. Fluorescence spectroscopy and multispectral imaging for fingerprinting of aflatoxin-B1 contaminated (Zea mays L.) seeds: a preliminary study. Sci. Rep. 12, 4849 https://doi.org/10.1038/s41598-022-08352-4.

Battilani, P., Toscano, P., Van der Fels-Klerx, H., Moretti, A., Camardo Leggieri, C., Brera, C., Rortais, A., Goumperis, T., Robinson, T., 2016. Aflatoxin B1 contamination in maize in Europe increases due to climate change. Sci. Rep. 6, 24328 https://doi.org/10.1038/srep24328.

Benkerrroum, N., 2020. Chronic and acute toxicities of aflatoxins: mechanisms of action. Int. J. Environ. Res. Public Health 17 (2), 423. DOI:10.3390/ijerph17020423.

Bertani, F.R., Businaro, L., Gambacorta, L., Mencattini, A., Brenda, D., Di Giuseppe, D., De Ninno, A., Solfrizzo, M., Martinelli, E., Gerardino, A., 2020. Optical detection of aflatoxins B in grained almonds using fluorescence spectroscopy and machine learning algorithms. Food Control 112, 107073. https://doi.org/10.1016/j.foodcont.2019.107073.

Bhat, R., Reddy, K.R.N., 2017. Challenges and issues concerning mycotoxins contamination in oil seeds and their edible oils: Updates from last decade. Food Chem. 215, 425–437. https://doi.org/10.1016/j.foodchem.2016.07.161.

Chakraborty, S.K., Mahanti, N.K., Mansuri, S.M., Tripathi, M.K., Kotwaliwale, N., Jayas, D.S., 2021. Nondestructive classification and prediction of aflatoxin-B1 concentration in maize kernels using Vis–NIR (400–1000 nm) hyperspectral imaging. J. Food Sci. Technol. 58, 437–450. https://doi.org/10.1007/s13197-020-04552-w.

Commission Regulation (EC), 2006. EUR-Lex - 02006R1881—20180319 - EN - EUR-Lex. [WWW Document]. Comm. Regul. No 1881/2006 19 December 2006 Doc. 02006R1881—20180319. URL ⟨https://eur-lex.europa.eu/legal-content/EN/TXT/?uri=CELEX%3A02006R1881—20220503⟩ accessed 17–02-2023.

FDA. Guidance for Industry: Action Levels for Poisonous or Deleterious Substances in Human Food and Animal Feed | FDA [WWW Document], (2000). URL URL ⟨https://www.fda.gov/regulatory-information/search-fda-guidance-documents/guidance-industry-action-levels-poisonous-or-deleterious-substances-human-food-and-animal-feed#afla⟩ accessed 17–02-2023.

Fernández-Ibañez, V., Soldado, A., Martínez-Fernández, A., de la Roza-Delgado, B., 2009. Application of near infrared spectroscopy for rapid detection of aflatoxin B1 in maize and barley as analytical quality assessment. Food Chem. 113 (2), 629–634. https://doi.org/10.1016/j.foodchem.2008.07.049.

Georgoulas, S., Bourgos, P., Tosic, M., Hintschich, S., Bertani, F.R., Tsakanikas, P., Gross, B., Alewijn, M., Martinelli, E., 2019. Food Analysis for All: The PhasmaFOOD Project Approach- Smart Systems Integration. 13th Int. Conf. Exhib. Integr. Issues Miniat. Syst. 1–8.

Gonzalez, R.C., Woods, R.E., 2007. Image Processing. Digital Image Processing Sect.2.1. Pearson Editions.

Groß, B., Hintschich, S., Tosic, M., Bourgos, P., Tsoumanis, K., Bertani, F.R., 2019. PhasmaFOOD - a miniaturized multi-sensor solution for rapid, non-destructive food quality assessment. OCM 2019 - Optical Characterization of Materials: Conference Proceedings. KIT Scientific Publishing, Karlsruhe, Karlsruhe, Germany, pp. 99–110.

Han, Z., Gao, J., 2019. Pixel-level aflatoxin detecting based on deep learning and hyperspectral imaging. Comput. Electron. Agric. 164, 104888. DOI: 10.1016/j.compag.2019.104888.

He, K., Zhang, X., Ren, S., Sun, J., 2016. Deep residual learning for image recognition. Proc. IEEE Conf. Comput. Vis. Pattern Recognit. 770–778.

Hussein, H.S., Brasel, J.M., 2001. Toxicity, metabolism, and impact of mycotoxins on humans and animals. Toxicology 167 (2), 101–134. https://doi.org/10.1016/s0300-483x(01)00471-1.

IARC, (1993). Monographs on the evaluation of carcinogenic risks to humans, Vol. 56.

Jallow, A., Xie, H., Tang, X., Qi, Z., Li, P., 2021. Worldwide aflatoxin contamination of agricultural products and foods: from occurrence to control. Compr. Rev. Food Sci. Food Saf. 20 (3), 2332–2381. DOI: 10.1111/1541-4337.12734.

Kimuli, D., Wang, W., Lawrence, K.C., Yoon, S.-C., Ni, X., Heitschmidt, G.W., 2018. Utilisation of visible/near-infrared hyperspectral images to classify aflatoxin B1 contaminated maize kernels. Biosyst. Eng. 166, 150–160. https://doi.org/10.1016/j.biosystemseng.2017.11.018.

Köppen, R., Koch, M., Siegel, D., Merkel, S., Maul, R., Nehls, I., 2010. Determination of mycotoxins in foods: current state of analytical methods and limitations. Appl. Microbiol. Biotechnol. 86 (6), 1595–1612. https://doi.org/10.1007/s00253-010-2535-1.

Liu, T.-H., Ehsani, R., Toudeshki, Zou A., X.-J, Wang, H.-J., 2019. Identifying immature and mature pomelo fruits in trees by elliptical model fitting in the Cr–Cb colour space. Precis. Agric. 20, 138–156. https://doi.org/10.1007/s11119-018-9586-1.

Lunadei, L., Ruiz-Garcia, L., Bodria, L., Guidetti, R., 2013. Image-based screening for the identification of bright greenish yellow fluorescence on pistachio nuts and cashews. Food Bioprocess Technol. 6, 1261–1268.

McLachlan, G.J., 2004. Discriminant Analysis and Statistical Pattern Recognition. Wiley Interscience. ISBN 978-0-471-69115-0. MR 1190469.

Pareek, C.M., Singh, N., Tewari, V.K., Dhruw, L.K., Dayananda Singh, H., 2023. Classification of broken maize kernels using artificial neural network-assisted image-processing approach. J. Biosyst. Eng. 48, 55–68. https://doi.org/10.1007/s42853-022-00173-7.

Poynton, C.A., 1996. A Technical Introduction to Digital Video. John Wiley & Sons, Inc, p. 175.

Pügner, T., Knobbe, J., Grüger, H., 2016. Near-infrared grating spectrometer for mobile phone applications. Appl. Spectrosc. 70, 734–745, 2016.

Ravikanth, L., Jayas, D.S., White, N.D.G., Field, P.G., Da-Wen Sun, D.-W., 2017. Extraction of spectral information from hyperspectral data and application of

hyperspectral imaging for food and agricultural products. Food Bioprocess Technol. 10, 1–33. https://doi.org/10.1007/s11947-016-1817-8.

Russakovsky, O., Deng, J., Su, H., Krause, J., Satheesh, S., Ma, S., Huang, Z., Karpathy, A., Khosla, A., Bernstein, M., Berg, A.C., Fei-Fei, L., 2015. ImageNet large scale visual recognition challenge. Int. J. Comput. Vis. (IJCV) Vol 115 (Issue 3), 211–252.

Singh, J., Mehta, A., 2020. Rapid and sensitive detection of mycotoxins by advanced and emerging analytical methods: a review. Food Sci. Nutr. 8 (5), 2183–2204. https://doi.org/10.1002/fsn3.1474.

Tao, F., Yao, H., Hruska, Z., Burger, L.W., Rajasekaran, K., Bhatnagar, D., 2018. Recent development of optical methods in rapid and non-destructive detection of aflatoxin and fungal contamination in agricultural products. TrAC Trends Anal. Chem. 100, 65–81. https://doi.org/10.1016/j.trac.2017.12.017.

Weidenbörner, M., 2001. Heidelberg. Encyclopedia of Food Mycotoxins. Springer Berlin. https://doi.org/10.1007/978-3-662-04464-3.

Wu, Q., Xu, H., 2020. Design and development of an on-line fluorescence spectroscopy system for detection of aflatoxin in pistachio nuts. Postharvest Biol. Technol. 159, 111016 https://doi.org/10.1016/j.postharvbio.2019.111016.

Wu, Q., Xie, L., Xu, H., 2018. Determination of toxigenic fungi and aflatoxins in nuts and dried fruits using imaging and spectroscopic techniques. Food Chem. 252, 228–242. https://doi.org/10.1016/j.foodchem.2018.01.076.

Zhang, X., Zhou, X., Lin, M., Sun, J., 2017. ShuffleNet: an extremely efficient convolutional neural network for mobile devices. arXiv preprint arXiv 1707.

Zhongzhi, H., 2019. Pixel-Level Aflatoxin Detection Based on Deep Learning and Hyperspectral Imaging. Computer Vision-Based Agriculture Engineering. CRC Press, pp. 69–81.

Zhongzhi, H., Limiao, D., 2020. Aflatoxin contaminated degree detection by hyperspectral data using band index. Food Chem. Toxicol. (1), 137. https://doi.org/10.1016/j.fct.2020.111159.

Zhou, Q., Huang, W., Liang, D., Tian, X., 2021. Classification of aflatoxin B1 concentration of single maize kernel based on near-infrared hyperspectral imaging and feature selection. Sensors 21, 4257. DOI:10.3390/s21134257.

Zhu, F., Yao, H., Hruska, Z., Kincaid, R., Brown, R., Bhatnagar, D., Cleveland, T., 2016. Integration of fluorescence and reflectance visible near-infrared (vnir) hyperspectral images for detection of aflatoxins in corn kernels. Trans. ASABE 59 (3), 785–794.

Zivoli, R., Gambacorta, L., Perrone, G., Solfrizzo, M., 2014. Effect of almond processing on levels and distribution of aflatoxins in finished products and byproducts. J. Agric. Food Chem. 62, 5707–5715. https://doi.org/10.1021/jf5018548.

Zweig, M.H., Campbell, G., 1993. Receiver-operating characteristic (ROC) plots: a fundamental evaluation tool in clinical medicine. Clin. Chem. 39 (4), 561–577. Erratum in: Clinical Chemistry 1993 Aug;39(8):1589. PMID: 8472349.